

# The chiral magnetic nanomotors†

Konstantin I. Morozov<sup>\*a</sup> and Alexander M. Leshansky<sup>ab</sup>Cite this: *Nanoscale*, 2014, 6, 1580

Received 5th August 2013

Accepted 5th November 2013

DOI: 10.1039/c3nr04853e

www.rsc.org/nanoscale

Propulsion of chiral magnetic nanomotors powered by a rotating magnetic field is in the focus of the modern biomedical applications. This technology relies on strong interactions of dynamic and magnetic degrees of freedom of the system. Here we study in detail various experimentally observed regimes of the helical nanomotor orientation and propulsion depending on the actuation frequency, and establish the relation of these two properties to the remanent magnetization and geometry of the helical nanomotors. The theoretical predictions for the transition between the regimes and nanomotor orientation and propulsion speed are in excellent agreement with available experimental data. The proposed theory offers a few simple guidelines towards the optimal design of the magnetic nanomotors.

## Introduction

The development of micro- and nano-robots that can be remotely actuated, navigated and delivered to a given location within the human body is a leading objective of the modern biomedical applications.<sup>1</sup> The idea of using the external magnetic fields for *in vitro* and *in vivo* micromanipulation was recognized long ago with the development of ferrofluids or colloidal solutions of magnetic nanoparticles.<sup>2</sup> For a long time, however, the magnetic drug targeting was achieved by the traditional technique based on applying the *gradient* magnetic field.<sup>3</sup> Despite some progress in this field, the method proved to be not very effective and convenient primarily due to the need to operate with large gradients of the applied field. The situation has changed dramatically with the development of the fundamentally new approach to the directed transport of magnetic particles. It was demonstrated<sup>4–6</sup> that the rotating magnetic field even of small or moderate amplitude can be applied for propulsion of *chiral* magnetic nanoparticles. These particles are named “artificial bacterial flagella” due to their biomimetic helical shape that provides chirality necessary for propulsion.<sup>5</sup>

The typical propulsion velocities offered by the new technique prove to be four to five orders of magnitude higher than those achieved by the gradient methods (see scaling arguments in the ESI†). It is not surprising that in the past few years the new technique has attracted considerable attention.<sup>7–10</sup> Physically, the dynamics of chiral magnetic nanomotors involve two

interrelated phenomena of magnetic and hydrodynamic nature, respectively. It was found in experiments<sup>7,8</sup> that at low frequency of the rotating magnetic field the helices wobble about the axis of the field rotation and their propulsion is hindered. However, upon increasing the field frequency, the wobbling gradually diminishes and a corkscrew-like propulsive motion takes over. Therefore a general search for the optimal nanomotor design should address the questions of the optimal choice of magnetic materials, magnetization procedure and helical geometry. In the recent investigation<sup>11</sup> one particular aspect of the problem was addressed, namely, shape optimization of the swimmer geometry maximizing the propulsion velocity at given applied magnetic torque assuming a perfect alignment of the helix along the axis of the field rotation. In the present study we establish the deep interrelation between the hydrodynamic and magnetic counterparts of the problem and show how it affects the dynamics of nanomotors.

## Magnetized helix in rotating magnetic field: problem formulation

Only two components of magnetization, because  $H$  (vector) has only two components?

Lets consider the behavior of magnetized helix in a rotating magnetic field. We assume that the longitudinal and transverse components of helix magnetization are fixed and equal to  $m_{||}$  and  $m_{\perp}$ , respectively. We will consider the problem in two different coordinate frames – in the laboratory coordinate system (LCS) fixed in space and in the body-fixed coordinate system (BCS) rigidly attached to the cylinder enclosing the helix. We study helix behavior in the externally imposed rotating uniform magnetic field  $H$ . We assume that in the LCS the field rotates in the horizontal plane

$$H = H(\cos \omega t, \sin \omega t, 0),$$

$H$  is the value of the uniform field (cos,sin,0) is the vector!

where  $H$  and  $\omega$  are, correspondingly, the field amplitude and its frequency. Specifying both coordinate systems, we will follow

<sup>a</sup>Department of Chemical Engineering, Technion – Israel Institute of Technology, Haifa 32000, Israel. E-mail: mrk@technion.ac.il

<sup>b</sup>Technion Autonomous System Program (TASP), Haifa 32000, Israel

† Electronic supplementary information (ESI) available: Effectiveness of the rotating magnetic field vs. the gradient field for particle propulsion, rotation matrix definition, stability analysis of the low-frequency solution, estimates of the rotational viscous resistance coefficients of helix, helical geometries, numerical algorithm of chirality calculation and remanent magnetization of helices. See DOI: 10.1039/c3nr04853e

the notation given in the book.<sup>12</sup> The coordinate axes of the systems are  $XYZ$  and  $x_1x_2x_3$ , respectively. We choose  $x_1$  and  $x_3$  axes of the BCS along the magnetization vectors  $\mathbf{m}_\perp$  and  $\mathbf{m}_\parallel$ , thus the magnetic moment  $\mathcal{M}$  of the helix in the BCS has a form

$$\mathcal{M}^{\text{BCS}} = (m_\perp, 0, m_\parallel), \quad \text{why } x_1 \text{ and } x_3? \quad (2)$$

The orientation of the BCS relatively to the LCK is determined by the Euler angles  $\varphi$ ,  $\theta$  and  $\psi$  (ref. 12) shown in Fig. 1.

The magnetized helix is engaged in a rotational motion driven by the magnetic torque  $\mathbf{L}_m = \mathcal{M} \times \mathbf{H}$ . This torque is a source of both rotational and translational movements of the particle. In the Stokes approximation, the helix motion is governed by the balance of external and viscous forces and torques acting on the particle<sup>14</sup>

$$0 = \xi \cdot \mathbf{U} + \mathcal{B} \cdot \boldsymbol{\Omega} \quad \text{Force balance in 3D} \quad (3)$$

B: Coupling tensor due to diagonal flagella?

$$\mathbf{L}_m = \mathcal{B}^T \cdot \mathbf{U} + \kappa \cdot \boldsymbol{\Omega} \quad \text{Newton (Drallsa)} \quad (4)$$

where  $\mathbf{U}$  and  $\boldsymbol{\Omega}$  are the translational and angular velocities of the helix,  $\xi$ ,  $\kappa$  and  $\mathcal{B}$  are the translational, rotational and coupling viscous resistance tensors, respectively.<sup>14</sup> We have also assumed in eqn (3) that there is no external force acting on the helix.

The formal solution of the problem can be readily obtained from eqn (3) and (4):

$$\mathbf{U} = -\xi^{-1} \cdot \mathcal{B} \cdot \boldsymbol{\Omega}, \quad \boldsymbol{\Omega} = \kappa_{\text{eff}}^{-1} \cdot \mathbf{L}_m, \quad \text{Speed depending either on rotation or torque} \quad (5)$$

where  $\kappa_{\text{eff}} = \kappa - \mathcal{B}^T \cdot \xi^{-1} \cdot \mathcal{B}$  is the re-normalized viscous rotation tensor.

The symmetries of the viscous resistance tensors allow us to split the problem of the helix dynamics into two separate parts: (i) rotational motion of an *achiral* slender particle (*i.e.*  $\mathcal{B} = 0$  and diagonal  $\kappa$  with components  $\kappa_{11} = \kappa_{22} = \kappa_\perp$ , *e.g.* rod) and (ii) translation of a *chiral* particle rotating with a prescribed angular velocity. In the following sections we consider both problems, while the arguments in support of such decomposition are provided in the “Concluding remarks” section.

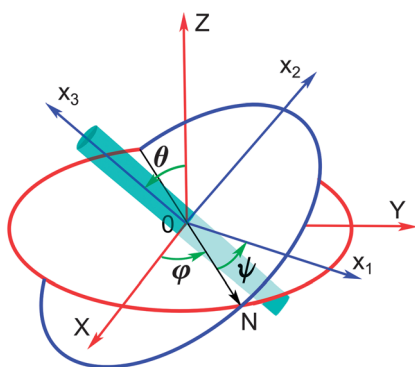


Fig. 1 The laboratory and body-fixed coordinate systems with the corresponding axes  $XYZ$  and  $x_1x_2x_3$  and the definition of the Euler angles  $\varphi$ ,  $\theta$  and  $\psi$ . For simplicity, the cylindrical envelope of a helix is shown.

## Magnetized cylinder in a rotating magnetic field

“write”?

It is convenient to right down the equation of the rotational motion (the second equation in eqn (5)) in the body-fixed coordinate system in which the tensor  $\kappa$  is a diagonal one. The components of the magnetic field (1) in the BCS are determined from the relation  $\mathbf{H}^{\text{BCS}} = \mathbf{R} \cdot \mathbf{H}$ , where  $\mathbf{R}$  is the rotation matrix<sup>13</sup> (see ESI†). Using data for the components of the angular velocity  $\boldsymbol{\Omega}$  (ref. 12) and elements of the rotation matrix, the torque balance equation takes a form:

$$Ac_{\varphi-\omega t} - Bs_{\varphi-\omega t}c_{\psi}s_{\theta} = \dot{\varphi}s_{\theta}, \quad (6)$$

$$As_{\varphi-\omega t}c_{\theta} + Bs_{\varphi-\omega t}s_{\psi}s_{\theta} = \dot{\theta}, \quad (7)$$

$$-C(c_{\varphi-\omega t}s_{\psi} + s_{\varphi-\omega t}c_{\psi}c_{\theta}) = \dot{\varphi}c_{\theta} + \dot{\psi}. \quad (8)$$

Here  $A = m_\parallel H/\kappa_\perp$ ,  $B = m_\perp H/\kappa_\perp$ , and  $C = m_\perp H/\kappa_\parallel$  are the three characteristic frequencies of the problem. We assume an arbitrary relationship between the variables  $m_\parallel$  and  $m_\perp$ , while  $\kappa_\parallel < \kappa_\perp$ , which is typical for a slender particle. We also use the compact notation, *i.e.*  $s_\psi = \sin \psi$ ,  $c_\theta = \cos \theta$ , *etc.* and the dot stands for the time derivative.

Generally, an overdamped dynamics of magnetic particles in a rotating magnetic field can be realized *via synchronous* and *asynchronous* regimes.<sup>15,16</sup> The synchronous regime is observed when there is a constant phase-lag between the Euler angle  $\varphi$  of the particle body and the external magnetic field  $\mathbf{H}$  while the angles  $\theta$  and  $\psi$  do not depend on time:

$$\varphi - \omega t \equiv \tilde{\varphi} = \text{const}, \quad \psi = \text{const}, \quad \theta = \text{const}. \quad (9)$$

Despite the complex form, the system (6)–(8) admits a simple analytical solution in the synchronous regime. Indeed, substituting the ansatz (9) into (6)–(8) yields the following algebraic system

$$Ac_{\tilde{\varphi}} - Bs_{\tilde{\varphi}}c_{\psi}s_{\theta} = \omega s_{\theta}, \quad (10)$$

$$s_{\tilde{\varphi}}(Ac_{\theta} + Bs_{\psi}s_{\theta}) = 0, \quad (11)$$

$$-C(c_{\tilde{\varphi}}s_{\psi} + s_{\tilde{\varphi}}c_{\psi}c_{\theta}) = \omega c_{\theta}. \quad (12)$$

Let us further consider the solutions of this system in detail.

### Synchronous regime: low-frequency solution

This obvious solution corresponds to the following values of the Euler angles:  $\psi = 0$ ,  $\theta = \pi/2$ . For these values eqn (11) and (12) are satisfied identically, whereas eqn (10) reduces to a relation for the phase angle  $\tilde{\varphi}$ :

$$Ac_{\tilde{\varphi}} - Bs_{\tilde{\varphi}} = \omega. \quad (13)$$

The solution of the last equation is

$$\tilde{\varphi} = \varphi_0 - \arcsin(\omega/\omega_c^{(1)}), \quad (14)$$

where  $\omega_c^{(I)} = \sqrt{A^2 + B^2}$  and  $\varphi_0$  is the angle between the total magnetic moment  $\mathcal{M}$  of the particle and its transverse component  $\mathbf{m}_\perp$  (see Fig. 2): its cosine is given by  $c_{\varphi_0} = B/\sqrt{A^2 + B^2} = m_\perp/\sqrt{m_\perp^2 + m_\parallel^2}$ .

This solution corresponds to a rod rotation about its short axis in the field plane, *i.e.*, the angle  $\theta$  between the long axis  $x_3$  of the cylinder and the axis  $Z$  of the magnetic field rotation is equal to  $\pi/2$  (see panel A in Fig. 2). The solution is physically clear. Indeed, in the low-frequency regime the variations of the rod orientation in space take place quasistatically: each instant the magnetic moment  $\mathcal{M}$  of the rod follows the external magnetic field  $\mathbf{H}$  with some slight phase-lag. Thus, both vectors  $\mathcal{M}$  and  $\mathbf{H}$  prove to be normal to the vector  $\boldsymbol{\omega}$  of the field rotation.

This is the low-frequency solution of the problem. It belongs to the limiting interval of field frequencies  $[0, \omega_c^{(I)}]$ . When,  $\omega = \omega_c^{(I)}$  the synchronous regime switches to the asynchronous one.<sup>16</sup> The simplest way to understand this effect is to consider behavior of the angle  $\alpha$  between the vectors  $\mathcal{M}$  and  $\mathbf{H}$ . Generally, the cosine of this angle reads

$$c_\alpha = \frac{\mathcal{M} \cdot \mathbf{H}}{\mathcal{M}H} = c_{\varphi_0}(c_\psi c_{\tilde{\varphi}} - s_\psi s_{\tilde{\varphi}} c_\theta) + s_{\varphi_0} s_{\tilde{\varphi}} s_\theta. \quad (15)$$

For the low-frequency solution with  $\psi = 0$ ,  $\theta = \pi/2$  it reduces to

$$c_\alpha^{(I)} = c_{\varphi_0} c_{\tilde{\varphi}} + s_{\varphi_0} s_{\tilde{\varphi}} = c_{\varphi_0 - \tilde{\varphi}} = \sqrt{1 - \left(\frac{\omega}{\omega_c^{(I)}}\right)^2}, \quad (16)$$

where we took into account eqn (14). Therefore,  $\omega_c^{(I)}$  is the maximal field frequency of the synchronized plane rotation of the rod. When  $\omega = \omega_c^{(I)}$ , the angle between vectors  $\mathcal{M}$  and  $\mathbf{H}$  achieves its maximal value of  $\pi/2$  and so the magnetic torque  $L_m$ . A further increase of the field frequency leads to the breakdown of the synchronous rotation of the rod since the viscous forces can no longer balance the magnetic forces.

The solution we found, however, is not unique. There is an additional solution that branches from the present one at the finite value of frequency  $\omega = A$ , *i.e.*, prior to transition to the asynchronous regime. This solution will be called the high-frequency branch.

## Synchronous regime: high-frequency solution

The high-frequency solution is characterized by the Euler angle  $\tilde{\varphi} = 0$ . From the system (10)–(12) one obtains<sup>18</sup>

$$s_\theta = \frac{A}{\omega}, \quad s_\psi = -\frac{\omega}{C} c_\theta = -\frac{\sqrt{\omega^2 - A^2}}{C}. \quad (17)$$

The angle between the vectors  $\mathcal{M}$  and  $\mathbf{H}$  reads

$$c_\alpha^{(II)} = c_{\varphi_0} c_\psi = \frac{B \omega_c^{(II)}}{C \omega_c^{(I)}} \sqrt{1 - \left(\frac{\omega}{\omega_c^{(II)}}\right)^2}, \quad (18)$$

where  $\omega_c^{(II)} = \sqrt{A^2 + C^2}$ . Since we assumed  $\kappa_\parallel < \kappa_\perp$ , then  $B < C$ , and  $\omega_c^{(I)} < \omega_c^{(II)}$ . Similarly to the analysis above,  $\omega_c^{(II)}$  is the maximal frequency of the synchronous rotation found for high-frequency solution.

Which of these two synchronous solutions is selected at high frequencies? To clarify this question qualitatively, let us consider two main limiting geometries shown in Fig. 2. In the low-frequency regime, the horizontal plane of field rotation coincides with the plane formed by the magnetization vectors  $\mathbf{m}_\perp$  and  $\mathbf{m}_\parallel$ . The vector of the total magnetic moment  $\mathcal{M} = \mathbf{m}_\perp + \mathbf{m}_\parallel$  follows the external magnetic field  $\mathbf{H}$  in an attempt to instantaneously catch up with it and, thereby, *minimizing the magnetic energy* of the rotating rod. Taking into account eqn (15) and (16) the magnetic energy of the rod in the low-frequency regime reduces to

$$E_{\text{magn}}^{(I)} = -\mathcal{M} \cdot \mathbf{H} = -\sqrt{(m_\perp^2 + m_\parallel^2)H^2 - \omega^2 \kappa_\perp^2}. \quad (19)$$

In the high-frequency regime, the energy minimization is achieved differently: the disadvantageous orientation of the longitudinal component  $\mathbf{m}_\parallel$  ( $\mathbf{m}_\parallel \perp \mathbf{H}$ ) is compensated by the energy gain due to reduced viscous friction associated with rotation about the long axis, compared to rotation about the short axis in the low-frequency regime,

$$E_{\text{magn}}^{(II)} = -\mathbf{m}_\perp \cdot \mathbf{H} = -\sqrt{m_\perp^2 H^2 - \omega^2 \kappa_\parallel^2}. \quad (20)$$

Assuming for simplicity that  $\kappa_\perp \gg \kappa_\parallel$ , we estimate the minimal value of the frequency  $\omega \approx m_\parallel H / \kappa_\perp = A$  starting from which the second regime becomes energetically favorable.

It should be emphasized however that in the above simplified analysis we assumed the orientation of the rod in the high-frequency regime to be vertical and ignored all the intermediate orientations. Actually, the high-frequency solution branches continuously from the low-frequency regime. Nevertheless, the above simplified analysis shows that the transition occurs at  $\omega = A$  in agreement with our estimate.

The aforementioned conclusion found from qualitative reasoning is confirmed also by the rigorous stability analysis (see ESI†). It is interesting to note also that the lower values of dissipation correspond to the high-frequency solution in comparison with that for the low-frequency one.

Thus, the following scenario of the phenomenon can be pictured. In the low-frequency regime,  $0 < \omega < A$ , the rod keeps rotating synchronously in the plane of the applied magnetic field. At higher frequencies also,  $A < \omega < \sqrt{A^2 + C^2}$ , the rod

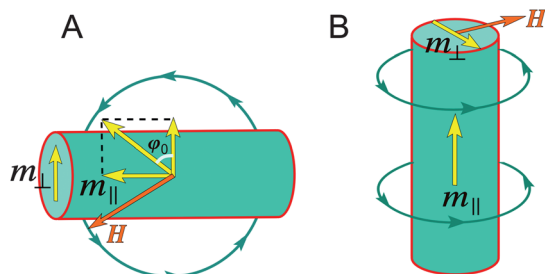


Fig. 2 Two limiting geometries of the rod orientation relative to the axis of magnetic field rotation. (A) and (B) indicate low- and high-frequency regimes, respectively. To simplify the estimates in high-frequency domain we assume  $\theta \approx 0$ , *i.e.*, the vertical orientation of the rod.

rotates synchronously, while the precession/wobbling angle  $\theta$  between the long axis of the rod and the Z-axis of the field rotation diminishes with the increase in frequency. The minimal angle  $\theta_{\min}$  is attained at  $\omega = \omega_c^{(II)}$

$$(s_\theta)_{\min} = \frac{A}{\omega_c^{(II)}} = \frac{1}{\sqrt{1 + \left(\frac{\kappa_\perp m_\perp}{\kappa_\parallel m_\parallel}\right)^2}} \quad (21)$$

At  $\omega = \omega_c^{(II)}$  the angle  $\alpha$  between  $\mathcal{M}$  and  $\mathbf{H}$  and the Euler angle  $\psi$  attain their extremum  $\alpha = -\psi = \pi/2$  and at even higher frequencies,  $\omega > \omega_c^{(II)}$ , the high-frequency solution breaks down and the synchronous regime switches to the asynchronous one.

Finally, we note that the anticipated scenario of transitions between various regimes was observed for the first time in experiments<sup>19</sup> where the cylinder was magnetized only transversely, *i.e.*,  $m_\parallel = 0$ . In the magnetic field rotating horizontally the cylinder is oriented vertically at high frequencies. The favorable at low frequencies horizontal orientation of the heavy rod was due to the action of gravity mimicking the longitudinal magnetization  $m_\parallel$  in our theory.

### Transition from wobbling to non-wobbling propulsion

Let us determine the limiting value of the aspect ratio of helices for non-wobbling propulsion. Following ref. 7 we choose a condition  $\theta_{\min} \leq \theta^* = 5^\circ$  as a wobbling/non-wobbling transition threshold. Using eqn (21) this condition reduces to the relation between the rotational viscous resistance coefficients

$$\frac{\kappa_\perp}{\kappa_\parallel} \geq \frac{\tan \varphi_0}{\tan \theta^*} \quad (22)$$

We approximate a helix by the enclosing prolate spheroid with the aspect ratio  $a/b$ , where  $a$  and  $b$  stand for the major and minor semi-axis, respectively. The explicit expressions for the rotational friction coefficients  $\kappa_\perp$  and  $\kappa_\parallel$  are given in the ESI.†

The condition in eqn (22) yields the boundary separating wobbling and non-wobbling propulsion at the step-out frequency  $\omega_c^{(II)}$  as a function of the aspect ratio  $a/b$  and the angle  $\varphi_0$  between the total magnetic moment  $\mathcal{M}$  of the helix and its transverse component  $\mathbf{m}_\perp$  (see Fig. 3). Note that below the curve in Fig. 3 the non-wobbling propulsion in the synchronous regime is inaccessible, while above the curve the non-wobbling propulsion (*i.e.* with  $\theta \leq 5^\circ$ ) can take place at frequencies below  $\omega_c^{(II)}$  depending on  $a/b$  and  $\varphi_0$ . Obviously, upon increasing the magnetization angle  $\varphi_0$  the limiting aspect ratio at the wobbling/non-wobbling transition also increases, *i.e.* a more slender helix is required to prevent wobbling. For example, for  $\varphi_0 = 45^\circ$  (*i.e.*, for equal values of the longitudinal and transverse magnetization), this ratio is  $a/b = 7.2$  whereas for the magnetization angle  $\varphi_0 = 10^\circ$  we have  $a/b = 2.13$ .

### Asynchronous regime

In the asynchronous regime all the Euler angles are time-dependent,  $\tilde{\varphi} = \tilde{\varphi}(t)$ ,  $\psi = \psi(t)$ ,  $\theta = \theta(t)$ , and the complete set of eqn (6)–(8) should be considered. The system is complex and the analytical solution is not feasible. Meanwhile, it admits a

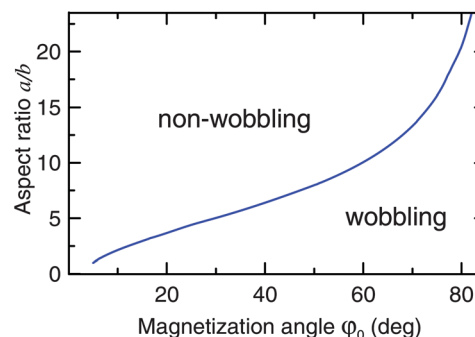


Fig. 3 Diagram showing wobbling and non-wobbling propulsion regimes as a function of helix aspect ratio  $a/b$  and the angle  $\varphi_0$  between the total magnetic moment  $\mathcal{M}$  of the helix and its transverse component  $\mathbf{m}_\perp$ . The solid line corresponds to propulsion with the wobbling angle of  $5^\circ$  attained at the step-out frequency.

quite simple approximation. We shall present here a heuristic approach to the solution of the problem and postpone the detailed analysis to future work.

The key element of our approach to the solution of the dynamical system (6)–(8) at  $\omega > \omega_c^{(II)}$  is the different character of time dependence of the three Euler angles. It follows from eqn (6) and (7) that the variables  $\tilde{\varphi}(t)$  and  $\theta(t)$  are involved in oscillatory motion. The characteristic frequency  $\Omega_{\text{osc}}$  of oscillations is estimated easily at  $\omega \geq \omega_c^{(II)}$  linearizing eqn (6) and (7) around their limiting values (17) in the synchronous regime. It proves to be equal to  $\Omega_{\text{osc}} = C\sqrt{1 - B/C} \approx C$ . At the same time, eqn (8), determining the dependence  $\psi(t)$  describes the appearance of the phase-lag of particle rotation from the rotating magnetic field. The characteristic frequency  $\Omega_{\text{lag}}$  of this phase-lag is proportional to the supercriticality,  $\Omega_{\text{lag}} \sim C\sqrt{1 - \omega_c^{(II)}/\omega}$ , (see below eqn (26)). Thus, at least in the vicinity of the critical frequency,  $\Omega_{\text{osc}} \gg \Omega_{\text{lag}}$ , *i.e.*, the angles  $\tilde{\varphi}(t)$  and  $\theta(t)$  can be considered as ‘fast’ variables, whereas  $\psi(t)$  as a ‘slow’ one. Since we are interested only in the long-time dynamics, we can eliminate the fast variables by time-averaging of eqn (6)–(8). First eqn (6) and (7) reduce after coarsening again to eqn (10) and (11) with the only difference that instead of the dynamical variables  $\tilde{\varphi}(t)$  and  $\theta(t)$  their time-averaged values  $\bar{\varphi}(t)$  and  $\bar{\theta}(t)$  are used. The solution of these equations is similar to that considered in the previous section:

$$\bar{\varphi} = 0, \quad s_{\bar{\theta}} = \frac{A}{\omega} \quad (23)$$

Using (23) in eqn (8) governing the dynamics of the slow variable  $\psi(t)$  reduces to

$$\dot{\psi} = -\omega c_{\bar{\theta}} - Cs_{\psi} \quad (24)$$

This is a standard form of the dynamical equation describing plane rotation of a magnetic moment in rotating magnetic field. It can be integrated analytically<sup>15,16</sup> to give

$$\psi(t) = -2\arctan \left[ \gamma + \sqrt{1 - \gamma^2} \tan \left( \frac{\sqrt{1 - \gamma^2}}{2} \omega c_{\bar{\theta}} t \right) \right], \quad (25)$$



where  $\gamma = C/(\omega c_\theta) = C/\sqrt{\omega^2 - A^2}$ . The sign minus in the right hand side of eqn (25) means that the magnetic moment of particles lags behind the magnetic field  $\mathbf{H}$ .

The average value of the rotation frequency lag is obtained as  $\Omega_{\text{lag}} = \bar{\dot{\psi}} = \lim_{T \rightarrow \infty} (1/T) \int_0^T \dot{\psi} dt$  where  $T$  is the period<sup>17</sup> and results in

$$\Omega_{\text{lag}} = -\sqrt{\omega^2 - \omega_c^{(II)2}} = -\sqrt{\omega^2 - A^2 - C^2}, \quad (26)$$

This completes the analysis of the rotational movement of the magnetized rod. Let us next consider the problem of the translational motion of the helix actuated by the rotating external magnetic field.

## Propulsion of the magnetized helix

The translational motion (propulsion) of the rotating helix is due to its chirality, *i.e.*, to non-zero coupling resistance matrix  $\mathbf{B}$  (see eqn (5)). For simplicity we consider only the helices with chirality along their axis, *i.e.*, in the BCS the single non-zero coefficient of  $\mathbf{B}$  is  $B_{\parallel}$ . Therefore an  $x_3$ -projection of the translational velocity of the helix is  $U_3^{\text{BCS}} = -(\mathcal{B}_{\parallel}/\xi_{\parallel})\Omega_3$ . In the LCS the velocity of the helix is  $\mathbf{U} = \mathbf{R}^T \cdot \mathbf{U}^{\text{BCS}}$ , where  $\mathbf{R}^T$  is the transposed rotation matrix.<sup>13</sup>  $\Omega_3$  is expressed in terms of the Euler angles as  $\Omega_3 = \dot{\phi}c_\theta + \dot{\psi}$ .<sup>12</sup> Thus the translational velocity of the helix in the rotating magnetic field is

$$\mathbf{U} = -(s_\phi s_\theta, -c_\phi s_\theta, c_\theta)(\dot{\phi}c_\theta + \dot{\psi})\mathcal{B}_{\parallel}/\xi_{\parallel} \quad (27)$$

Let us consider the most relevant propulsion for the  $Z$ -component of the velocity for regimes considered above.

### Low-frequency synchronous regime

Since  $\theta = \pi/2$  the propulsion velocity is zero by symmetry,  $U_Z = 0$ .

### High-frequency synchronous regime

From eqn (17) we obtain

$$U_Z = -\omega c_\theta^2 \mathcal{B}_{\parallel}/\xi_{\parallel} = -\omega[1 - (A/\omega)^2]\mathcal{B}_{\parallel}/\xi_{\parallel} \quad (28)$$

### Asynchronous regime

From eqn (23) and (26) one finds

$$U_Z = -\omega \left(1 - \frac{A^2}{\omega^2}\right) \left(1 - \sqrt{1 - \frac{C^2}{\omega^2 - A^2}}\right) \mathcal{B}_{\parallel}/\xi_{\parallel}. \quad (29)$$

The ratio of the corresponding resistance coefficients in (28) and (29),  $\mathcal{B}_{\parallel}/\xi_{\parallel}$ , can be determined, *e.g.*, numerically. We used the particle-based algorithm<sup>26</sup> to compute the resistance coefficients for three different types of helices. The helices differ by the orientation of their filament cross-section, assumed to be elliptical, relatively to the helix axis. For *normal* and *binormal* helices the filament cross-section is elongated, correspondingly, perpendicularly and along the helical axis (see ESI† for details). Geometric illustration of these both types of helices is provided

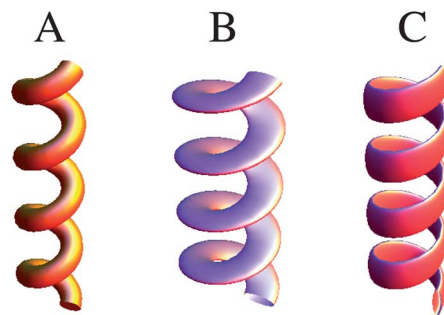


Fig. 4 Illustration of the regular (A), normal (B) and binormal (C) helical propellers.

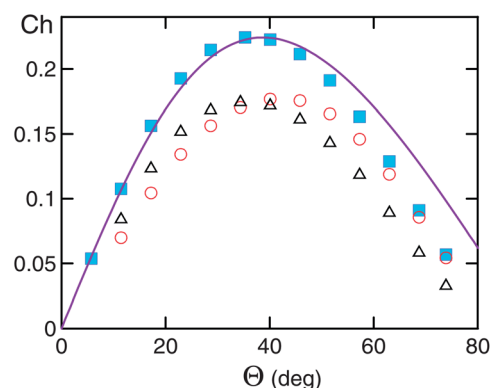


Fig. 5 The chirality coefficient  $\text{Ch} = -\mathcal{B}_{\parallel}/(\xi_{\parallel}R)$  vs. the helical angle  $\Theta$  for regular (circular cross-section, filled squares), normal (circles) and binormal (triangles) helices. The solid line stands for the RFT prediction.

in Fig. 4B and C, respectively. The degenerate case of a *regular* helix corresponds to a filament with circular cross-section (see Fig. 4A). The dimensionless chirality coefficient  $\text{Ch} = -\mathcal{B}_{\parallel}/(\xi_{\parallel}R)$  is depicted in Fig. 5 vs. the helical angle  $\Theta$  for regular (squares), normal (circles) and binormal (triangles) helices. For all three types of helices their radius is  $R/r = 4$ , where  $2r$  is the characteristic filament thickness.<sup>27</sup> The cross-sectional aspect ratio for normal and binormal helices is set to 1 : 2 and the length-to-width ratio for all filaments is  $L/2r = 30$ .

The solid line in Fig. 5 stands for the prediction of the local Resistive Force Theory (RFT) corrected for the finite width of the filament. It can be readily seen that the regular helix is a better propeller than normal and binormal helices, however at large enough  $\Theta \gtrsim 60^\circ$  the normal helix is as good as the regular one. The optimal helical angle maximizing the propulsion speed is in the range  $\sim 35\text{--}40^\circ$ . The agreement between the RFT prediction and the numerical results (for a regular helix) is excellent up to  $\Theta \approx 40^\circ$ . The details of the numerical algorithm and the RFT derivation are provided in the ESI.†

## Comparison to experiments

The comparison of the theoretical prediction for the precession (wobbling) angle  $\theta$  in eqn (17) to the experimental results\* is

shown in Fig. 6 for the best-fit value of the critical frequency  $\nu_c = A = 11.5$  Hz. It can be readily seen that the experimental results are in excellent agreement with the proposed theory. The rightmost point in Fig. 6 corresponds to the experimentally determined step-out frequency  $\nu_{s-o} = \omega_c^{(II)}/2\pi = 54.5$  Hz (marked by the dotted line) at which the synchronous solution switches to the asynchronous one.

Let us estimate the limiting (minimal) value of the precession angle,  $\theta_{\min}$ , corresponding to  $\nu_{s-o}$ . As before, we approximate a helix by the prolate spheroid with the aspect ratio  $a/b = 4.5$ .<sup>8</sup> The corresponding ratio of the rotational viscous resistance coefficients is  $\kappa_{\perp}/\kappa_{\parallel} = 5.61$  (see ESI†). The ratio  $m_{\perp}/m_{\parallel}$  of the components of magnetization is determined by the angle  $\varphi_0$  (see Fig. 2). According to ref. 8, this angle equals to  $\approx 54^\circ$ , thus  $m_{\perp}/m_{\parallel} = \cot 54^\circ = 0.726$ . Substituting both these values into eqn (21) yields  $\theta_{\min} = 13.8^\circ$ . The theoretical estimate proves to be close to the experimental value of  $\theta_{\min} \approx 14^\circ$  found in (ref. 8) for the rightmost point in Fig. 6. A close estimate  $\theta_{\min} = 12.2^\circ$  can also be found from (21) using the best-fit frequency  $\nu_c = 11.5$  Hz and the experimentally measured value of  $\nu_{s-o} = 54.5$  Hz.

The comparison of the theory to the experimental results<sup>8</sup> for the propulsion velocity  $U_z$  is shown in Fig. 7. Fitting the experimentally measured propulsion velocity in the high frequency synchronous regime (the solid line in Fig. 7) to the theoretical prediction in eqn (28) we choose the value of the dimensional multiplicative coefficient  $2\pi B_{\parallel}/\xi_{\parallel}$  to be equal to  $0.08 \mu\text{m}$ . We determine the dimensionless ratio  $B_{\parallel}/(\xi_{\parallel}R)$  numerically as described in the ESI† and using the data reported in ref. 8, *i.e.*,  $R = 0.20 \mu\text{m}$  the radius of the helix,  $r = 0.17 \mu\text{m}$  for the radius of the filament,  $P = 1 \mu\text{m}$  for the helical pitch, so that the helical angle  $\Theta = \tan^{-1}(2\pi R/P) \approx 51.5^\circ$ . The computed value of the dimensional coefficient  $2\pi B_{\parallel}/\xi_{\parallel}$  is equal to  $0.094 \mu\text{m}$ , while for a slightly higher angle  $\Theta = 53.5^\circ$  we find  $2\pi B_{\parallel}/\xi_{\parallel} = 0.081 \mu\text{m}$  that perfectly fits the experimental results. It is worthy to also mention that the prediction for the propulsion velocity in the asynchronous regime in eqn (29) (the descending dashed line in Fig. 7) does not involve any adjustable parameters and fits very well the experimental data.

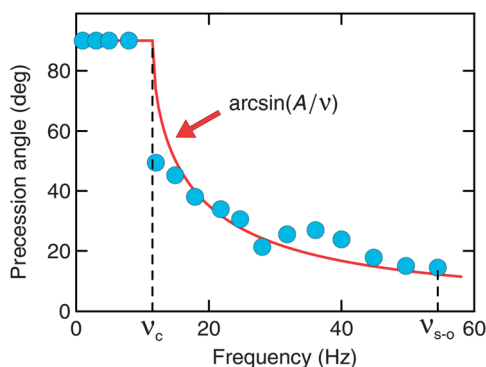


Fig. 6 Precession angle as a function of frequency  $\nu = \omega/2\pi$  of the rotating magnetic field. The experimental results (filled circles) are taken from ref. 8. The solid line is the theoretical prediction in eqn (17). The dashed lines denote the critical frequency  $\nu_c = 11.5$  Hz and the step-out frequency  $\nu_{s-o} = 54.5$  Hz.

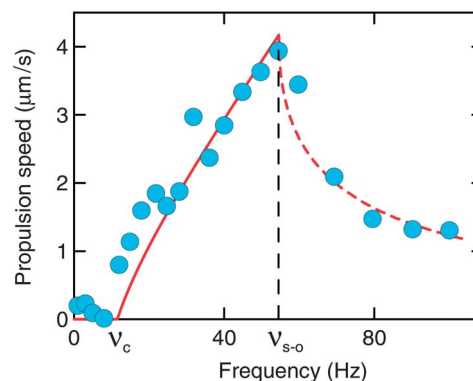


Fig. 7 Propulsion velocity of a helix as a function of frequency  $\nu = \omega/2\pi$  of the rotating magnetic field. The experimental results (filled circles) are taken from ref. 8. The ascending (solid) line  $f_1 = 0.08\nu(1 - \nu_c^2/\nu^2)$  and descending (dashed) line  $f_2 = f_1(1 - \sqrt{\nu^2 - \nu_{s-o}^2}/\sqrt{\nu^2 - \nu_c^2})$  are the theoretical predictions from eqn (28) and (29), respectively, with  $\nu_c = 11.5$  Hz and  $\nu_{s-o} = 54.5$  Hz.

## Magnetization of helices

In the preceding sections we studied the movement of the magnetized rod and/or helix in rotating magnetic field provided that the magnetization components  $m_{\perp}$  and  $m_{\parallel}$  are prescribed. In the present section we shall consider the general magnetic properties of the ferromagnetic helices.

The magnetism of helices is due to a thin layer ( $\leq 10$  nm) of a ferromagnetic material (Ni, Co, Fe or their derivatives and alloys) coating a magnetically neutral helical body. The magnetic properties of thin magnetic films are well studied in the case of *plane* films.<sup>20,21</sup> The shape of a thin film constrains the magnetization vector  $\mathbf{M}$  (the magnetic moment per unit volume) to lie in the plane of the film.<sup>20</sup> The films are found to be *uniaxially* anisotropic ones, *i.e.*, the magnetization vector  $\mathbf{M}$  aligns with an *easy* axis  $\mathbf{e}$  in the absence of the external magnetic field  $\mathbf{H}$ . The density  $f_a = E_a/V$  of the anisotropy energy is written in the form

$$f_a = K \sin^2(\widehat{\mathbf{M}}, \mathbf{e}), \quad (30)$$

where  $(\widehat{\mathbf{M}}, \mathbf{e})$  is an angle between the vectors  $\mathbf{M}$  and  $\mathbf{e}$  and  $K$  is an anisotropy constant. The absolute value  $M$  of the magnetization is known – it is equal to its saturation value at given temperature. We indicate these values for three major magnetics at room temperature:  $M_{\text{Ni}} = 480$  G,  $M_{\text{Fe}} = 1700$  G, and  $M_{\text{Co}} = 1400$  G.

The appearance of this in-plane anisotropy depends strongly on the film preparation conditions. There are three possible factors affecting the anisotropy: (1) short-range directional order of magnetic atoms during their deposition, (2) angle of incidence between the substrate and the depositing beam, and (3) anisotropic strain and other properties of the substrate.<sup>20,22</sup> This is why the anisotropy is called *induced* one *vs.* the uniaxial magneto-crystalline *bulk* anisotropy. In particular, the induced magnetic anisotropy typically proves to be an order of magnitude lower than its bulk value. Let us indicate the values of  $K$  for three most common magnetics:  $K_{\text{Ni}} = (1 \div 3) \cdot 10^3 \text{ erg cm}^{-3}$  and

$K_{\text{Ni}}^{\text{bulk}} = 5 \times 10^4 \text{ erg cm}^{-3}$  for nickel;<sup>21</sup>  $K_{\text{Fe}} = 3 \times 10^4 \text{ erg cm}^{-3}$  and  $K_{\text{Fe}}^{\text{bulk}} = 4.5 \times 10^5 \text{ erg cm}^{-3}$  for iron;<sup>23</sup>  $K_{\text{Co}} = 4 \times 10^5 \text{ erg cm}^{-3}$  and  $K_{\text{Co}}^{\text{bulk}} = 4 \times 10^6 \text{ erg cm}^{-3}$  for cobalt.<sup>24</sup>

The minimization of the sum  $f_a + f_m$  of the anisotropy energy and magnetic energy  $f_m = -\mathbf{M} \cdot \mathbf{H}$  determines the equilibrium orientation of vector  $\mathbf{M}$  in the combined field resulting from the external magnetic field  $\mathbf{H}$  and the anisotropy field  $\mathbf{H}_a = (2K/M)\mathbf{e}$ .<sup>20</sup> The anisotropy field  $H_a$  defines the characteristic value of the external magnetic field required for film re-magnetizing. The characteristic values of the anisotropy field are  $H_a^{\text{Ni}} \sim 10 \text{ Oe}$ ,  $H_a^{\text{Fe}} \sim 30 \text{ Oe}$ , and  $H_a^{\text{Co}} \sim 500 \text{ Oe}$ . The measured values of the anisotropy fields are mainly in agreement with the above estimate, however, they can scatter notably depending on the way of sample preparation. For example,  $H_a$  of permalloy (Fe–Ni alloy) can vary from 1 to 50 Oe.<sup>22</sup> Analogously, in the recent study<sup>25</sup> the in-plane uniaxial magnetic anisotropy field of a multilayer cobalt film was found to be in the range from 150 to 900 Oe.

As we already mentioned, these results hold for the plane magnetic films. To the best of our knowledge there is no data for the ferromagnetic films of helicoidal geometry. Thus, aiming to estimate the *remanent magnetization* of magnetic helices, we have to use the data obtained for the plane films under some additional assumptions. We assume that (a) the magnetic layer covering the helix has a constant thickness; (b) the helix is composed of an integer number of turns; (c) the cross-section of the helical filament is asymmetric. For simplicity, we also suppose that the magnetic structure of the film is formed by an ensemble of magnetic domains with the easy magnetization axes  $\mathbf{e}$  determined by the helix geometry. We consider two possible orientations of the easy axis: (i)  $\mathbf{e}$  is the vector tangent to the centreline of the helix; (ii)  $\mathbf{e}$  is directed along the longer cross-sectional axis of the helix. For the latter case we have to consider two different geometries – normal and binormal helix. The details of calculations are given in the ESI.† Here we provide only the final results for different particular cases.

*Easy axis is tangent to the centreline of the helix.* We describe here the result for the longitudinal  $m_{\parallel}$  and transversal  $m_{\perp}$  components of the remanent magnetization appeared after removal of external field  $\mathbf{H} = H(\sin \alpha, 0, \cos \alpha)$  which forms the angle  $\alpha$  with the axis of the helix. Both values are given in the units of the magnetic moment  $M_s v$  of a hypothetical plane layer with the same volume  $v$  of the magnetic material, where  $M_s$  is its saturation magnetization. The final result depends on two angles – the helix angle  $\Theta$  and the magnetizing angle  $\alpha$ . For low values  $\alpha$  of the angle between the field  $\mathbf{H}$  and the helix,  $0 < \alpha < \pi/2 - \Theta$ , the transversal component is absent:

$$\hat{m}_{\parallel} = \cos \Theta, \quad \hat{m}_{\perp} = 0. \quad (31)$$

For high values  $\alpha > \pi/2 - \Theta$  there are both components:

$$\hat{m}_{\parallel} = \frac{2}{\pi} \cos \Theta \arcsin P, \quad \hat{m}_{\perp} = \frac{2}{\pi} \sin \Theta \sqrt{1 - P^2}, \quad (32)$$

where  $P = \cot \alpha \cot \Theta$ . The result is shown in Fig. 8. We note that eqn (32) holds for both normal and binormal helices.

*Easy axis is along the longer cross-sectional axis of the normal helix.* This case of the normal helix with easy axis in the

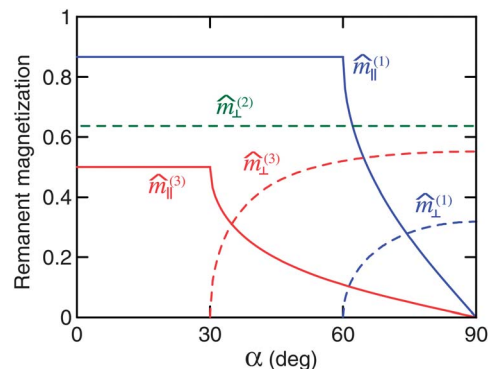


Fig. 8 The dimensionless longitudinal  $\hat{m}_{\parallel}$  (solid lines) and transversal  $\hat{m}_{\perp}$  (dashed lines) components of the remanent magnetization as a function of the angle between the magnetizing field and the helix axis. Indexes correspond to three cases considered in the text. The results are shown for the helix angle  $\Theta = 30^\circ$ . In the case of the 'dual' helix with the angle  $\Theta = 60^\circ$ , one finds the 'dual' solution: the lines sub-indexed 1 and 3 interchange. For the helix with  $\Theta = 45^\circ$  the lines sub-indexed 1 and 3 merge. The curve  $\hat{m}_{\perp}^{(2)}$  remains unaltered for any value of  $\Theta$ .

direction of the longer cross-sectional axis is the simplest one. The result does not depend on the orientation  $\alpha$  of the magnetizing field, and there is only single (transversal) nontrivial component of magnetization:

$$\hat{m}_{\parallel} = 0, \quad \hat{m}_{\perp} = 2/\pi. \quad (33)$$

*Easy axis is along the longer cross-sectional axis of the binormal helix.* There are also cases corresponding to small and large values of the angle  $\alpha$ , respectively. For small angles  $\alpha < \Theta$  there exists only the longitudinal magnetization:

$$\hat{m}_{\parallel} = \sin \Theta, \quad \hat{m}_{\perp} = 0. \quad (34)$$

For high values of  $\alpha > \Theta$  there are both components

$$\hat{m}_{\parallel} = \frac{2}{\pi} \sin \Theta \arcsin G, \quad \hat{m}_{\perp} = \frac{2}{\pi} \cos \Theta \sqrt{1 - G^2}, \quad (35)$$

where  $G = \cot \alpha \tan \Theta$ . We note that the results for cases 1 and 3 are dual to each other, namely, eqn (31) and (32) found for some value  $\Theta = \Theta^*$  of the helix angle are identical to eqn (34) and (35) corresponding to the dual helix with the helix angle  $\Theta_{\text{dual}} = \pi/2 - \Theta^*$ .

We consider here the idealized case of prescribed orientation of the easy axes of magnetic domains. In practice, there is a distribution of the easy axes in the plane film and therefore a combined result is found for the limiting cases. So, the magnetization of the normal helix proves to be a weighted result of cases 1 and 2. For the binormal helix, it is a combination of cases 1 and 3.

## Concluding remarks

To conclude, we developed a theory of externally driven propulsion of chiral magnetic nanomotors. The compact analytical expressions for the wobbling angle and the propulsion velocity,

obtained for all (*i.e.* synchronous and asynchronous) regimes in a wide range of driving field frequency, show excellent agreement with previously reported experimental results (see Fig. 6 and 7).

This theory relies on splitting the problem into two separate parts: (i) rotational motion of an *achiral* slender particle (*e.g.* a rod) and (ii) translation of a *chiral* particle rotating along its long axis. To justify such decomposition, let us consider the re-normalized viscous rotation resistance tensor  $\kappa_{\text{eff}}$  introduced in eqn (5). Firstly, the contribution of the re-normalization of  $\kappa$  due to translation concerning the diagonal element  $\kappa_{||}$  (corresponding to rotation about the helical axis  $x_3$ ) can be estimated as  $\kappa_{||\text{eff}} \sim \kappa_{||}(1 - \text{Ch}^2)$ . Since the dimensionless chirality coefficient  $\text{Ch} \lesssim 0.2$  (see Fig. 5), one can safely assume  $\kappa_{||\text{eff}} \approx \kappa_{||}$ . Secondly, the rotation tensor  $\kappa$  of the *finite* helix is nearly diagonal and the *principal rotation axis* (corresponding to the lowest eigenvalue of the  $\kappa$ ) slightly deviates from the  $x_3$  axis. The approximate value of this misalignment angle  $\beta$  between the principal axes of rotation and the helical axis  $x_3$  can be readily found using symmetries of the rotation tensor as  $\cos \beta \approx 1 - \kappa_{23}^2/2(\kappa_{11} - \kappa_{33})^2$ . For example, our particle-based computations reveal that for a helix with radius  $R/r = 3$ , helical angle  $\Theta = 57.3^\circ$  and 3 full turns, we found  $\beta \approx 2.96^\circ$ . Obviously,  $\beta$  diminishes as the number of helical turns increases. It is also worth mentioning that this misalignment should result in an apparent longitudinal magnetization  $\sim m_\perp \sin \beta$  and wobbling even for a purely transversely magnetized helix. Note also that in the BCS aligned with the principal rotation axis, the transverse components  $\kappa_{11}$  and  $\kappa_{22}$  of the finite helix are not identically equal, but this discrepancy was proved to be negligible and had no effect on the dynamics.

The developed theory also offers a few simple guidelines towards the optimal design of chiral magnetic nanomotors. An effective steering of nanomotors should be obtained when they possess the maximal transverse magnetization  $m_\perp$  and minimal longitudinal magnetization  $m_{||}$ . For a prescribed value of magnetization angle  $\varphi_0$  between the total magnetic moment  $\mathcal{M}$  of the nanomotor and its transverse component  $\mathbf{m}_\perp$ , there is a critical slenderness of the helix at which propulsion is accompanied by an arbitrarily small wobbling (*e.g.*  $\theta \leq 5^\circ$  at the step-out frequency, see Fig. 3). The vanishing value of  $m_{||}$  (*i.e.* in the BCS aligned with the principal rotation axis) allows complete prevention of wobbling for all driving frequencies and maximizes the propulsion velocity of nanomotors,  $U_{\text{max}} \sim (m_\perp H/\eta V) R \text{Ch}$ , with  $V$  being the propeller volume. Since  $m_\perp \sim M_s v$ , the best propellers are those (i) composed of magnetics with high value of the saturation magnetization  $M_s$  and (ii) magnetized transversally. In the typical experimental setups, the magnitude of the driving magnetic field is  $\sim 10$  Oe ( $\sim 1$  mT), which is comparable with the anisotropy field  $H_a$  of nickel. For example, nickel-coated helices may undergo re-magnetization in the course of steering diminishing its propulsion efficiency. Thus, (iii) the use of nanomotors coated with hard magnetics (*e.g.* cobalt) with high value of the anisotropy field  $H_a$ , (iv) magnetized initially in a strong magnetic field ( $\sim 1$  T) and driven by a weaker rotating field, is preferable. The preferable geometry of helical nanomotors is probably the *normal* helix (v): the slightly lower value of chirality

Ch in comparison to the regular helix (see Fig. 5) is well compensated by the larger value of the magnetization as shown in Fig. 8. The optimal helix angle is in the range  $\Theta = 35^\circ \div 45^\circ$  maximizing the chirality,  $\text{Ch} \approx 0.2$  (vi). Despite a large variability in the nanofabrication techniques and experimental setups,<sup>4–10,19</sup> it is interesting to point out that one of the pioneering experimental studies in this field<sup>4</sup> has empirically adopted most of the rules formulated above.

## Acknowledgements

The authors would like to thank Ambarish Ghosh, Li Zhang and Soichiro Tottori for providing details of the experiments with chiral magnetic nanomotors and Peer Fischer and Oded Kenneth for useful discussion. This work was partially supported by the Japan Technion Society Research Fund (A.M.L.) and by the Israel Ministry for Immigrant Absorption (K.I.M.).

## Notes and references

- 1 K. E. Peyer, L. Zhang and B. J. Nelson, *Nanoscale*, 2013, **5**, 1259–1272.
- 2 R. E. Rosensweig, *Ferrohydrodynamics*, Cambridge University Press, Cambridge, 1985.
- 3 A. S. L  bbe, C. Alexiou and C. Bergemann, *J. Surg. Res.*, 2001, **95**, 200–206.
- 4 A. Ghosh and P. Fischer, *Nano Lett.*, 2009, **9**, 2243–2245.
- 5 L. Zhang, J. J. Abbott, L. Dong, B. E. Kratochvil, D. Bell and B. J. Nelson, *Appl. Phys. Lett.*, 2009, **94**, 064107.
- 6 L. Zhang, J. J. Abbott, L. X. Dong, K. E. Peyer, B. E. Kratochvil, H. X. Zhang, C. Bergeles and B. J. Nelson, *Nano Lett.*, 2009, **9**, 3663–3667.
- 7 S. Tottori, L. Zhang, F. Qiu, K. K. Krawczyk, A. Franco-Oregon and B. J. Nelson, *Adv. Mater.*, 2012, **22**, 811–816.
- 8 A. Ghosh, D. Paria, H. J. Singh, P. L. Venugopalan and A. Ghosh, *Phys. Rev. E: Stat., Nonlinear, Soft Matter Phys.*, 2012, **86**, 031401.
- 9 K. E. Peyer, F. Qiu, L. Zhang and B. J. Nelson, IEEE International Conference on Intelligent Robots and Systems, 2012, art. no. 6386096, pp. 2553–2558.
- 10 A. Ghosh, P. Mandal, S. Karmakar and A. Ghosh, *Phys. Chem. Chem. Phys.*, 2013, **15**, 10817–10823.
- 11 E. E. Keaveny, S. W. Walker and M. J. Shelley, *Nano Lett.*, 2013, **13**, 531–537.
- 12 L. D. Landau and E. M. Lifshitz, *Mechanics*, Pergamon Press, Oxford, 3rd edn, 1976.
- 13 J. Diebel, *Representing Attitude: Euler Angles, Unit Quaternions, and Rotation Vectors*, Matrix, Citeseer, 2006.
- 14 J. Happel and H. Brenner, *Low Reynolds Number Hydrodynamics*, Kluwer, 1983.
- 15 C. Caroli and P. Pincus, *Phys. Kondens. Mater.*, 1969, **9**, 311–319.
- 16 A. C  bers and M. Ozols, *Phys. Rev. E: Stat., Nonlinear, Soft Matter Phys.*, 2006, **73**, 021505.
- 17 P. Tierno, J. Claret, F. Sagu  s and A. C  bers, *Phys. Rev. E: Stat., Nonlinear, Soft Matter Phys.*, 2009, **79**, 021501.



- 18 In the process of writing the paper, we became aware of the article 10 where the formal solution for the synchronous regime has also been found *via* an alternative approach.
- 19 P. Dhar, C. D. Swayne, T. M. Fischer, T. Kline and A. Sen, *Nano Lett.*, 2007, **7**, 1010–1012.
- 20 J. B. Goodenough and D. O. Smith, Magnetic properties of thin films, in *Structure and Properties of Thin Films*, ed. C. A. Neugebauer, Wiley, New York, 1959, pp. 112–126.
- 21 R. D. Soohoo, *Magnetic thin films*, Harper & Row Publishers, New York, 1965.
- 22 D. O. Smith, *J. Appl. Phys.*, 1959, **30**, 264S–265S.
- 23 T. G. Knorr and R. W. Hoffman, *Phys. Rev.*, 1959, **113**, 1039–1046.
- 24 T. Tanaka, M. Takahashi and S. Kadowaki, *J. Appl. Phys.*, 1998, **84**, 6768–6772.
- 25 J. Vergara, C. Favieres and V. Madurga, *Nanoscale Res. Lett.*, 2012, **7**, 577.
- 26 A. M. Leshansky, *Phys. Rev. E: Stat., Nonlinear, Soft Matter Phys.*, 2009, **80**, 051911.
- 27 For normal and binormal helices  $2r$  stands for the length of the cross-sectional minor axis.